Structural health monitoring payload for the MISSE platform on the International Space Station

Evgenii Volkov[a *], Thomas Pierson[a *], David Hunter[b], Seth Kessler[c], Andrei Zagrai[a]
[a]Department of Mechanical Engineering, New Mexico Institute of Mining and Technology, 801 Leroy Pl., Socorro, NM 87801 USA; [b]New Mexatronics LLC., Albuquerque, NM 87123 USA; [c]Metis Design Corporation, 205 Portland St, Boston, MA 02114
* Both authors contributed equally to this work

Abstract

A Structural Health Monitoring (SHM) payload was developed for integration into the Materials International Space Station Experiment (MISSE) to evaluate spacecraft structural integrity in low-Earth orbit. The system includes two instrumented aluminum plates: one for electromechanical impedance measurements using the Afalina miniaturized analyzer, and another for guided-wave propagation and defect detection via a notch and controlled bolt loosening. A shielded compartment houses data acquisition units, while passive experiments expose piezoelectric sensors to the space environment. Ground tests confirmed functionality of the payload. During six-month orbital operation, the payload aims to collect in-orbit SHM data to inform future intelligent spacecraft designs.

Keywords: SHM, ISS, PZT Wafers, Space vehicles, ISAM, OSAM, electromechanical impedance, guided waves.

Symposium: SPIE Smart Structures + Nondestructive Evaluation
Symposium Dates: 16 - 19 March 2026
Symposium Location: Vancouver, BC Canada

Manuscripts are due **25 February 2026**.

PAPER NUMBER: 13951-13

1. INTRODUCTION

1.1. *Continuing development towards reusable space vehicles*

Aerospace vehicles are routinely manufactured from riveted or bolted structural sections, a construction methodology that introduces fatigue crack initiation sites at fastener holes and joint interfaces[1]. As the space industry moves toward reusable launch vehicles and spacecraft to reduce per-mission costs [21], the ability to detect and localize structural damage in real time becomes increasingly important. Structural health monitoring (SHM) acts as a framework for detecting and localizing damage as it occurs in space vehicles, which enables informed maintenance decisions that extend vehicle service life and improve mission safety margins [22].

Piezoelectric wafer active sensors (PWAS) are well suited for space-based SHM due to their low mass, low power consumption, and the ability of piezoelectric wafers to both actuate and receive acoustic transmissions[2]. Two complementary PWAS-based SHM modalities are investigated in this work: guided wave propagation [23] and electromechanical impedance (EMI) sensing[3]. Together, these methods can form the basis of an acoustic smart structure capable of continuously monitoring damage along the surface of a spacecraft (Figure 1(a)), providing the actionable structural data needed to support vehicle safety and reusability. The experimental payload described in this paper will be deployed to the MISSE platform for a six-month orbital mission (Figure 1(b)).

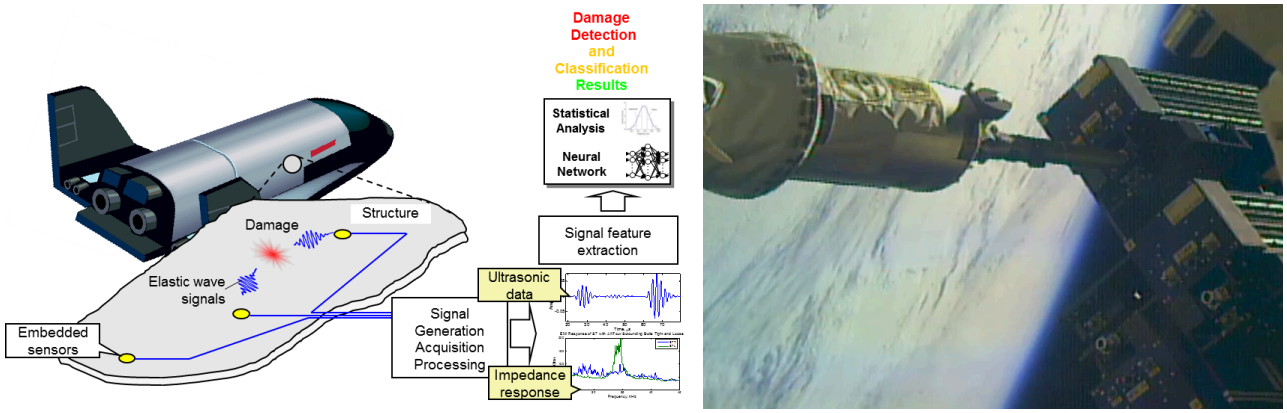

Figure 1. (a) Piezoelectric ceramic wafers can be implemented into a sensing skin along the surface of an aerospace vehicle. An array of wafers on sections of vehicle components can use elastic wave and EMI sensing to provide autonomous SHM and structural awareness. **(b)** The SHM experimental payload will be deployed to the Materials International Space Station Experiment (MISSE). The payload will autonomously run tests while connected to the platform over a 6-month mission.

1.2. *Application of modern SHM theory in orbit*

Despite significant on-Earth development of PWAS-based SHM, no prior in-orbit data exists characterizing guided wave propagation or lead zirconate titanate (PZT) wafer electromechanical behavior in the space environment. The combined effects of thermal cycling, ionizing radiation, hard vacuum, and microgravity on PZT transducer performance and acoustic wave propagation remain uncharacterized. This gap limits the certainty with which Earth-based SHM models can be applied to in-service spacecraft.

This paper presents a research payload designed to close that gap. The payload will be deployed to the International Space Station (ISS) via the Materials International Space Station Experiment (MISSE) platform in 2026, conducting a six-month data collection mission in low Earth orbit (LEO). Both passive and active SHM experiments are implemented on 1 mm-thick Aluminum 6061-T6 plate substrates. This aluminum alloy was chosen as a material representative of structural panels used in launch vehicles and spacecraft. Guided wave and EMI measurements will be

collected autonomously throughout the mission and compared against controlled laboratory baselines to isolate the effects of the LEO environment on PZT sensing performance.

2. PAYLOAD DESIGN

2.1. Detailed description of the payload

The experimental payload is organized into four vertically stacked structural layers, all machined from the same batch of Aluminum 6061-T6 to ensure material consistency. The overall assembly is shown in Figure 2, and the internal arrangement is detailed in Figure 3. The base layer provides a mechanical mounting interface to the MISSE platform dock. The experiment will be mounted with 6 M3 bolts, and is within size constraints of the MISSE experimental section. Above the mounting frame, the test plate layer houses two 1 mm-thick aluminum experimental plates, each secured within a quarter-inch rectangular frame using 60 M3.5 screws that impose a bolted boundary condition along all four edges. These test plates are the experimental layer of the payload, with the outermost plate exposed to the full LEO environment, facing away from the central ISS. The cross-sectional arrangement of the bolted frames and electronics compartment is shown in Figure 3(b).

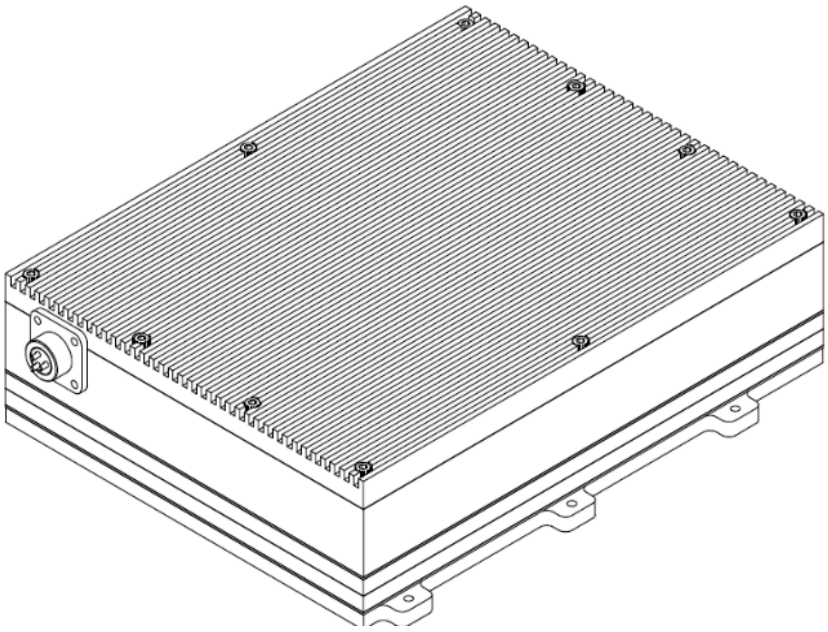

Figure 2. The complete payload assembly consists of 4 main sections stacked on top of one another: a mounting bracket for the MISSE platform, two bolted 1 mm thick aluminum test plates, an electronic housing cabin, and radiation shielding.

The lower test plate is dedicated to the guided wave experiment and is instrumented with five PWAS nodes. A synthetic crack is machined between two sensor locations to simulate mission crack fatigue damage. Two additional PWAS nodes are intentionally exposed to the full LEO environment outside the payload enclosure: one bonded to the face of the plate and one suspended freely above the exterior plate. These nodes will be used to characterize the effects of vacuum and radiation exposure on unprotected transducers. To study damage detection at structural joints, one of the 60 frame screws is left deliberately loosened below the torque rating of the other screws, and one screw is pre-cracked. These faulty screws simulate common fastener degradation modes in aerospace structures that are of concern for SHM studies. The upper test plate is dedicated to the EMI experiment and carries two square PWAS nodes, also secured within

a bolted frame of 60 M3.5 screws.. 16 screws are attached to each long edge, 12 to each short edge, and 4 at the corners, for a total of 60 fasteners per plate.

The third layer is an enclosed electronics cabin containing all components required for autonomous payload operation. Power is supplied from the ISS main frame at 24 V DC via a 3-pin circular industrial connector. The main power is distributed to all subsystems through two custom printed circuit boards (PCBs) designed in KiCad, which interface with every other circuit in the system. These boards route power to each component and include signal conditioning resistors for both guided wave and EMI measurement accuracy.

Guided wave excitation, data collection, and measurement timing cycle is managed by the Metis Design MD7 embedded controller, which is connected to each PWAS through 24 American Wire Gauge (AWG) coaxial cable. The MD7 controller provides 7 barrel connector ports for data collection.

EMI measurements are performed by the Afalina miniaturized impedance analyzer, powered at 5V. The incoming voltage is regulated from the 24 V bus using an adjustable LM2596 DC-DC step-down converter (HW-441), providing a stable 5 V supply without overloading the Afalina board. The Afalina is connected to the PWAS array on the second test plate through coaxial cable, and records EMI emission data on a small SD card. The Afalina includes an on-chip thermometer that records ambient temperature at each data collection event, enabling thermal correction for acoustic measurements.

A passive PZT characterization experiment is housed in the bottom corner of the electronics cabin, visible in Figure 3(a). Six unsoldered open-circuit PZT wafers suspended within a wire mesh, attached to an aluminum bracket inside of the cabin compartment. Measurements will be taken to classify each wafer before and after flight to quantify the net effect of the LEO environment on undriven piezoelectric ceramics in the protected enclosure.

The payload is topped by a finned aluminum heat spreader that promotes radiative thermal dissipation and provides additional radiation shielding for the underlying electronics. The finned radiator is half an inch thick, providing a half-inch boundary of aluminum in all directions for cabin electronics.

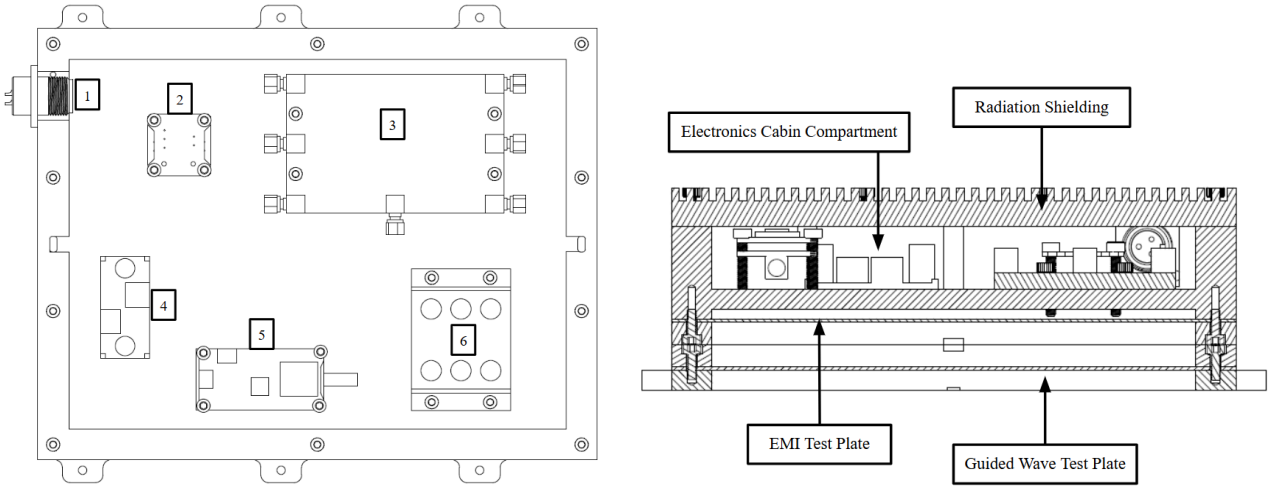

Figure 3. (a) Detailed view of electronics cabin compartment of payload. (1) 3-prong barrel connector to connect to ISS-MISSE power line. (2) PCB stack for power distribution to other electronics. (3) Metis Design MD7 microcontroller. (4) Voltage adapter/variable resistor for Afalina board. (5) Afalina miniaturized EMI analyzer. (6) Passive PZT wafer bracket and mesh. **(b)** Cross sectional view of payload. Guided wave and EMI test plates are mounted with 56 stainless steel fasteners each, with the fasteners facing opposite directions to establish fully bolted boundary conditions. Electronics in the cabin compartment are mounted with 3M fasteners with hex standoffs. Radiation shielding surrounds the cabin compartment on all sides.

2.2. Piezoelectric transducers

Active PWAS nodes used for guided wave testing are 7 mm diameter PZT ceramic discs. PZT wafers have high temperature resistance for piezoelectric performance, and enable stable and precise acoustic measurements. Each wafer consists of a ferroelectrically soft lead zirconate titanate core with lead-alloy electrodes on both faces. As illustrated in Figure 4, a wrap-around electrode configuration routes one electrode terminal to the top surface, allowing the wafer to be adhesively bonded to the test plate while both electrodes remain accessible for coaxial connection. EMI test wafers share the same wrap-around architecture but are square in geometry to provide a different modal response profile suited to impedance-based damage detection, rather than the circular shape.

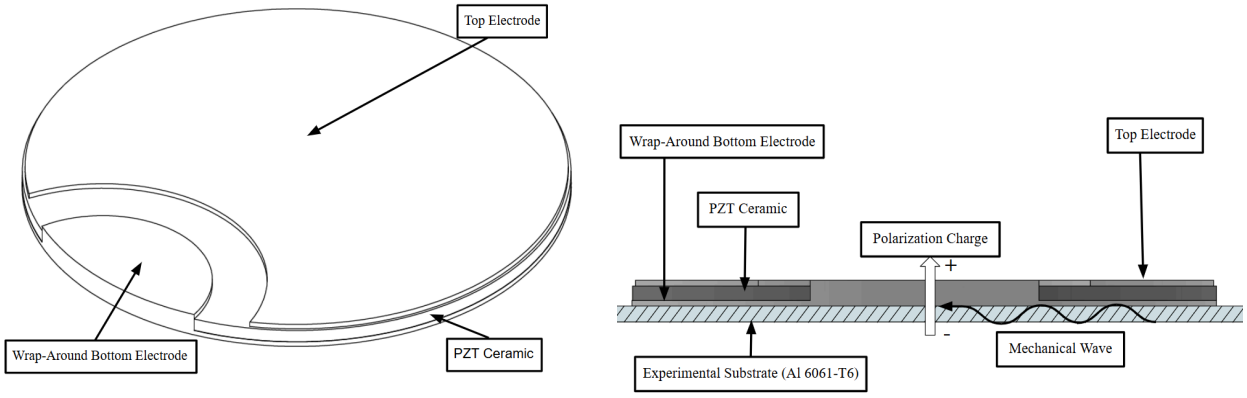

Figure 4. (a) Isometric and **(b)** side view of a 7 millimeter diameter, 0.25 millimeter thick PZT wafer. The PZT wafers used for guided wave and EMI classification consist of a flat PZT ceramic with lead-free electrodes on each side of the ceramic. The bottom electrode is wrapped around to the top of the PZT ceramic, so that both electrodes are accessible when the wafer is attached to an experimental substrate.

2.3. Environmental considerations

All structural components of the payload were machined from the same batch of 6061-T6 aluminum, ensuring regularity and somewhat isotropic properties for testing. All electrical components except for those intentionally left outside the payload are protected by half an inch of aluminum on all sides, providing some protection for the ionizing radiation of space. All screws, bolts, and other hardware are rated for the high vacuum environment, and are treated for corrosion resistance. Electronics have been validated to withstand thermal cycling in orbit.

Small channels are machined between sections of the payload to run cables between the electronics cabin compartment and the sensors on the test plates. These channels serve an additional purpose to allow for outgassing during the 6-month mission, as many of the electronics are composed of PCB layers prone to degradation. All solder used in the payload is of a lead-free silver based alloy rated for the space environment.

2.4. Hardware Description

2.4.1. Afalina - Miniaturized E/M Impedance Analyzer

Conventional electromechanical impedance (EMI) interrogation for structural health monitoring typically relies on bulky, laboratory-grade phase-gain analyzers, such as the Keysight E4990A or HP4192A. While earlier portable alternatives utilized the AD5933 integrated circuit, the advent of the advanced AD5941 chip has enabled the design of the Afalina, a novel, miniaturized impedance measurement system specifically tailored for aerospace payload constraints (Figure 5(1)). The foundational hardware architecture and schematic principles of this system were originally described by Hunter,[4] who developed the first-generation Afalina prototype for spacecraft SHM applications.. The current flight architecture consists of a central commercial off-the-shelf Arduino-compatible microcontroller paired with custom-designed, stackable channel boards. The ARM Cortex-M0 based microcontroller serves as the central hub, equipped with a battery management controller, micro-SD storage, and a USB interface. Each individual channel board

is powered by an independent low-noise linear regulator and contains an AD5941 chip, a dedicated crystal oscillator, high-precision calibration resistors, and hardware address pins.

At the core of the measurement hardware, the AD5941 integrates a digital-to-analog converter (DAC), a transimpedance amplifier (TIA), and a 16-bit analog-to-digital converter (ADC) operating at 1.6 megasamples per second[5]. Within the Afalina operational framework, the DAC synthesizes an excitation waveform spanning from 1 to 250 kHz. Following analog filtering and amplification, this signal is applied across the piezoelectric wafer active sensor (PWAS). The structural response, manifested as a return current drawn by the PWAS, is captured by the TIA, converted into a proportional voltage, and subsequently digitized by the ADC. The resulting digital data stream is processed through a cascade of sinc2 and sinc3 filters before entering an internal discrete Fourier transform (DFT) engine. By correlating the synthesized excitation signal with the measured input response, this on-chip DFT module directly calculates the complex electromechanical impedance.

To account for the extreme thermal fluctuations inherent to the LEO environment, The Afalina board is additionally equipped with a TMP117 high-precision digital temperature sensor. The TMP117 provides a 16-bit measurement resolution of 0.0078 °C and a maximum accuracy of ± 0.1 °C, operating reliably across a wide thermal range from –55 °C to +150 °C. Because the dielectric and mechanical properties of PZT transducers are highly temperature-dependent, continuous thermal logging precisely at the measurement node is critical. This localized temperature data is appended to each acquired impedance spectrum, providing the essential baseline for developing temperature-compensated SHM algorithms in orbit.

In the Afalina architecture, the MD7 microcontroller preloads a comprehensive sequence of measurement instructions directly into the internal sequencer of the AD5941 chip. Once the command queue is populated, the microcontroller issues a hardware trigger, prompting the impedance analyzer to autonomously execute its broad-spectrum excitation and sampling routines. The resulting high-resolution impedance spectra, alongside the synchronized TMP117 thermal data, are temporarily buffered within the onboard memory. Finally, this cached data is downloaded to the central microcontroller for non-volatile storage and eventual downlink. This sequencer-driven autonomy drastically minimizes the active processing overhead on the master microcontroller, ensuring highly reliable and power-efficient operation throughout the mission's duration.

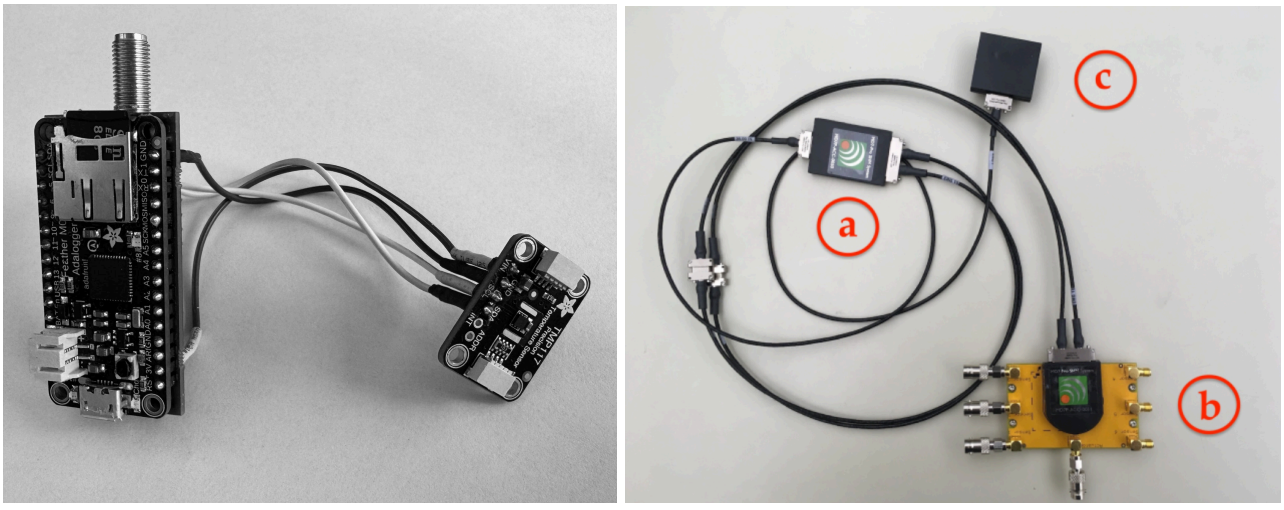

Figure 5. Miniaturized data acquisition hardware integrated into the ISS structural health monitoring payload. **(1)** The Afalina miniaturized electromechanical impedance analyzer, equipped with a TMP117 high-precision digital temperature sensor for concurrent thermal logging. **(2)** The MD7-pro microcontroller and data acquisition system, consisting of three primary components: **(a)** the accumulation node, capable of storing up to 8 GB of acoustic data; **(b)** the acquisition node, which collects signal data and features built-in signal processing; and **(c)** the USB converter interface for transferring data to an external computer.

2.4.2. MD7 Wave Propagation Hardware

The MD7-pro microcontroller (Figure 5(2)), developed by Metis Design Corporation, offers a method of performing on-board data acquisition tasks for SHM. The MD7-pro system has multiple advantages over other microcontrollers that are important for SHM performance: the system is lightweight, and is impervious to most electromagnetic interference. Effective SHM processing for aerospace vehicles must optimize for weight while still interrogating and collecting data, which the MD7-pro system enables. The MD7 system consists of a microprocessor, as well as three different nodes: an accumulation node for information processing, an acquisition node to collect signal data, and an analog sensor base. The MD7 system has flight history, and is computationally efficient through local signal processing and noise reduction.

2.5. Mission operational protocol

The payload is programmed to execute a complete test cycle approximately once every 7 days, yielding 24 individual measurement sessions over the six-month mission. Each cycle operates within a 600-minute timing window, initiated and sequenced by the internal clock of the Metis Design MD7 microcontroller.

Guided wave testing occupies the first 110 minutes of each window. During this interval, the MD7 sequentially excites one PWAS node and records acoustic response data from each of the remaining four nodes on the guided wave test plate. This procedure is repeated 20 times per session. Since one ISS orbit is completed in approximately 92 minutes, these measurements span a full orbital period and capture the associated thermal variation at distinct LEO locations.

EMI testing begins 6 hours after window initialization and runs for approximately 3 hours, during which the Afalina analyzer interrogates the EMI test plate 180 times. This duration covers roughly two complete orbital cycles, ensuring that the acquired impedance spectra sample the full range of ambient thermal conditions encountered in LEO.

3. ELECTROMECHANICAL IMPEDANCE SHM OF PAYLOAD STRUCTURE

3.1. Fixed-free beam model and experiment

To validate the boundary condition modeling for the flight payload, a 1D cantilever beam was investigated as a simplified 1D representation of the payload's primary sensing plate. The beam utilizes the exact same fastening hardware (bolt and clamping blocks) and edge distance as the flight configuration. This approach allows for isolating the complex compliance mechanics of the bolted joint in a simplified 1D domain before extending the analysis to the 2D plate model described in Section 3.2.

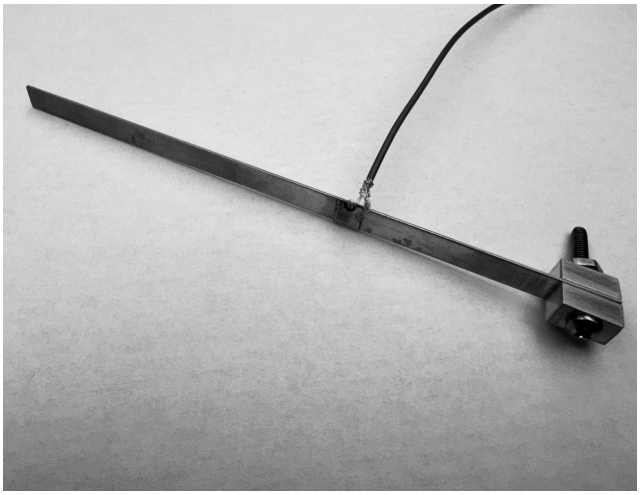

Figure 6. Photograph of the experimental cantilever beam specimen with bolted fixation. The beam is fabricated from Al6061-T6 aluminum alloy with an overall length of 165.1 mm (6.50 inches), a width of b = 7.01 mm (0.276 inches), and a thickness of h = 1.016 mm (0.040 inches). The nominal active vibrating length is L = 152.4 mm (6.00 inches), measured from the free end to the geometric clamp edge. An APC 850 piezoelectric wafer active sensor (PWAS), measuring 7.0 × 7.0 × 0.25 mm, is bonded to the top surface and centered at 2L/3 = 101.6 mm from the free end. The structure is secured using aluminum clamping blocks with a single M3.5 bolt to approximate a fixed boundary condition.

3.1.1. Theoretical Modal Analysis of Free-Fixed Cantilever Beam

3.1.1.1. Beam Configuration and Boundary Conditions

The electromechanical impedance experiment employs a free-fixed cantilever beam fabricated from aerospace-grade aluminum alloy Al6061-T6. The nominal dimensions and material properties at room temperature[6] are:

• Length: L = 152.4 mm (6.00 inches); Width: b = 7.01 mm; Thickness: h = 1.016 mm (0.040 inches)

• Young's modulus: E = 68.9 GPa; Mass density: ρ = 2700 kg/m³; Poisson's ratio: ν = 0.33

The beam is free (unconstrained) at x = 0 and fixed (clamped) at x = L via a bolted connection using two 0.5-inch-wide aluminum blocks. A Ø3.5 mm hole at x = 158.75 mm from the free end accommodates the fastener. A photograph of the beam assembly is shown in Figure 6. A square PZT sensor (APC 850, 7.0 × 7.0 × 0.25 mm) manufactured by APC International[7] is adhesively bonded to the beam surface at x_{sensor} = 2L/3 = 101.6 mm from the free end (equivalently, L/3 = 50.8 mm from the fixed end). APC 850 is a soft piezoelectric ceramic (Navy Type II equivalent) with density ρ_{PZT} = 7600 kg/m³ and Young's modulus Y_{11}^{E} = 63 GPa[7]. The sensor width matches the beam width (7.01 mm), creating a composite cross-section over the 7 mm bonding length. Despite its small size, the sensor introduces a 69% local mass increase and contributes significant rotary inertia through the parallel-axis (Steiner) effect, as discussed in Section 3.1.1.3. Electromechanical impedance measurements span the frequency range 200–32,200 Hz with 20 Hz resolution (1,601 data points).

3.1.1.2. Euler-Bernoulli Bending Theory

For small-amplitude transverse vibrations of a slender beam (h/L = 0.0067 ≪ 1), the Euler-Bernoulli equation provides a baseline model[8]:

$$EI\frac{\partial^4 w}{\partial x^4} + \rho A\frac{\partial^2 w}{\partial t^2} = 0 \tag{3.1}$$

where w(x,t) is the transverse displacement, E is Young's modulus, I = bh³/12 is the second moment of area, ρ is the mass density, and A = bh is the cross-sectional area.

Assuming harmonic motion w(x,t) = W(x)e^(iωt), the spatial equation becomes:

$$\frac{d^4 W}{dx^4} - \beta^4 W = 0, \quad \beta^4 = \frac{\rho A\omega^2}{EI} \tag{3.2}$$

The general solution is:

$$W(x) = C_1\cos(\beta x) + C_2\sin(\beta x) + C_3\cosh(\beta x) + C_4\sinh(\beta x) \tag{3.3}$$

For free-fixed boundary conditions:

• Free end (x = 0): M(0) = 0, V(0) = 0 → W″(0) = 0, W‴(0) = 0

• Fixed end (x = L): w(L) = 0, θ(L) = 0 → W(L) = 0, W′(L) = 0

Applying these four conditions yields the characteristic equation[9]:

$$\cos(\lambda)\cosh(\lambda) = -1 \tag{3.4}$$

where λ = βL is the dimensionless eigenvalue. The natural frequencies are:

$$f_n = \frac{\lambda_n^2}{2\pi L^2}\sqrt{\frac{EI}{\rho A}} \tag{3.5}$$

The eigenvalues λ_n are roots of Eq. (3.4), solved numerically: $\lambda_1 = 1.87510407$, $\lambda_2 = 4.69409113$, $\lambda_3 = 7.85475744$, $\lambda_4 = 10.99554073$, $\lambda_5 = 14.13716839$. For $n \geq 6$, the asymptotic approximation $\lambda_n \approx (2n-1)\pi/2$ is accurate to within 0.01%[9].

3.1.1.3. Timoshenko Beam Theory and FEM Implementation

The Euler-Bernoulli model assumes plane sections remain plane and perpendicular to the neutral axis, neglecting two physical effects that become significant at higher mode numbers: (1) rotary inertia — the kinetic energy associated with cross-sectional rotation; and (2) shear deformation — the deviation of the cross-section from perpendicularity due to transverse shear.

For a slender beam (h/L = 0.0067), these effects are small but measurable at high frequencies. The Timoshenko beam theory accounts for both phenomena through the coupled governing equations[10,11]:

$$\kappa GA\left(\frac{\partial^2 w}{\partial x^2} - \frac{\partial \psi}{\partial x}\right) = \rho A\frac{\partial^2 w}{\partial t^2} \tag{3.6a}$$

$$EI\frac{\partial^2 \psi}{\partial x^2} + \kappa GA\left(\frac{\partial w}{\partial x} - \psi\right) = \rho I\frac{\partial^2 \psi}{\partial t^2} \tag{3.6b}$$

where w is the transverse displacement, ψ is the rotation angle of the cross-section (independent of the beam slope $\partial w/\partial x$), κ is the shear correction factor, and G = E/[2(1+ν)] is the shear modulus. For rectangular cross-sections, the Cowper shear coefficient[12] is:

$$\kappa = \frac{10(1+\nu)}{12+11\nu} = 0.8509 \quad (\text{for } \nu = 0.33) \tag{3.7}$$

This value accounts for the non-uniform shear stress distribution across the rectangular cross-section and is appropriate for narrow beams (b/h ≈ 7) under plane-stress conditions[12]. The Timoshenko equations (6a–b) do not admit a closed-form frequency equation for arbitrary boundary conditions. Natural frequencies must therefore be determined numerically.

A finite element model was constructed using 320 two-node Timoshenko beam elements, each with four degrees of freedom (transverse displacement and rotation at each node). Each element employs the standard consistent stiffness and mass matrices that include both bending and shear stiffness contributions (through κGA), as well as both translational and rotational inertia terms[13].

The bonded PZT sensor is incorporated into the FEM as a distributed mass and stiffness patch over the 7 mm bonding region. For each finite element that overlaps with the sensor footprint, the element mass and stiffness matrices are augmented proportionally to the overlap fraction. Three contributions are included:

- Translational inertia: $\Delta(\rho A) = \rho_{PZT} \times b_{PZT} \times h_{PZT}$, where $\rho_{PZT} = 7600$ kg/m³, $b_{PZT} = 7.0$ mm $\approx b_{beam}$, and $h_{PZT} = 0.25$ mm. This adds 0.093 g distributed over 7 mm, representing a 69% local mass increase relative to the bare beam.
- Rotary inertia: $\Delta(\rho I) = \rho_{PZT} \times (I_{own} + A_{PZT} \times d^2)$, where d is the distance from the beam neutral axis to the PZT centroid. With the sensor bonded to the beam surface, $d = h_{beam}/2 + h_{PZT}/2 = 0.633$ mm. The Steiner (parallel-axis) term $A_{PZT} \times d^2 = 7.01$ mm^4 dominates over the PZT's own moment of area $I_{own} = bh^3/12 = 0.009$ mm^4, yielding a combined $\Delta(\rho I)$ that exceeds the bare beam's ρI by approximately 116% over the sensor region.
- Bending stiffness: $\Delta(EI) = E_{PZT} \times (I_{own} + A_{PZT} \times d^2)$, where $E_{PZT} = Y_{11}^E = 63$ GPa[7]. This stiffness contribution partially offsets the frequency reduction from the added inertia. At the sensor location, $\Delta(EI)/EI_{beam} \approx 106\%$, indicating that the PZT acts as a local stiffener of comparable magnitude to the host beam.

3.1.2. Comparison of theory and measurement.

Experimental EMI spectra were acquired over the frequency range 200–32,200 Hz with 20 Hz resolution (1,601 data points). Resonance peaks in the electrical resistance spectrum correspond to structural natural frequencies of the beam. Peak identification was performed using an adaptive sequential tracking algorithm: for each theoretical mode, the Timoshenko-predicted frequency at nominal geometry was used as a starting target, and the nearest local resistance maximum within a ±10% search window was selected. The correction factor from each matched peak was propagated forward to refine predictions for subsequent modes, improving robustness against cumulative drift.

17 bending modes predicted within the measurement range were identified in the experimental spectrum. Axial (longitudinal) modes at 8,287 Hz and 24,860 Hz were predicted theoretically but not included in the peak matching procedure. Although the surface-bonded PZT sensor, operating via the d_{31} piezoelectric effect, theoretically couples to both flexural and in-plane longitudinal deformations[2], the beam's longitudinal dynamic stiffness is significantly higher than its bending stiffness. Consequently, the electromechanical impedance signatures of the axial modes are comparatively weak, and no clear axial resonance peaks could be confidently identified in the experimental spectrum.

Frequency resolution filtering was applied to exclude modes where spectral discretization significantly limits measurement accuracy. Modes with relative resolution $\Delta f/f > 2\%$ (where $\Delta f = 20$ Hz is the frequency step) were removed from the quantitative comparison. This excluded Mode-2 (220 Hz, $\Delta f/f = 9.1\%$) and Mode-3 (600 Hz, $\Delta f/f = 3.3\%$) (omitted from the table 1), leaving 15 bending modes (Mode-4 through Mode-18) for analysis.

The mean absolute error over the 15 usable modes is 0.80%, with a maximum of 2.37% at Mode-6 (2960 Hz). The errors are predominantly positive across all modes, indicating systematic frequency overprediction. Since $f \propto 1/L^2$ for bending modes, this bias suggests the beam behaves as though slightly longer than the nominal 152.4 mm, motivating the effective length optimization of Section 3.1.3.

Table 1: Timoshenko + PZT Theory vs. Experimental Frequencies (Nominal L = 152.4 mm, PZT mass and stiffness included). Mean |Δ| (15 modes): 0.80% Max |Δ|: 2.37% (Mode-6)

Mode	f_{theory} [Hz]	f_{exp} [Hz]	Δ [%]	Δf/f [%]
4	1225	1220	+0.43	1.64
5	2027	2000	+1.34	1.00
6	3030	2960	+2.37	0.68
7	4218	4200	+0.43	0.48

8	5620	5580	+0.72	0.36
9	7232	7160	+1.01	0.28
10	8976	8880	+1.08	0.23
11	10980	10940	+0.37	0.18
12	13199	13140	+0.45	0.15
13	15463	15460	+0.02	0.13
14	18062	18020	+0.23	0.11
15	20875	20880	−0.02	0.10
16	23633	23680	−0.20	0.08
17	26808	26800	+0.03	0.07
18	30190	30320	−0.43	0.07

3.1.3. Optimization of beam effective length to match adequate BC

A bolted clamp transmits bending moment through friction and contact pressure over a finite area; the transition from free to fully restrained behavior is therefore gradual rather than abrupt. The effective fixity point — the location at which the beam may be considered rigidly clamped — consequently lies beyond the geometric clamp edge[1]. Rather than modeling the contact mechanics explicitly, L_{eff} is identified directly from the measured natural frequencies via a single-parameter optimization. The objective function is a weighted mean absolute relative error:

$$J(L) = \sum_i w_i |\Delta_i(L)| \tag{3.8}$$

where $\Delta_i(L) = [f_{theory,i}(L) - f_{exp,i}] / f_{exp,i}$ is the relative error for mode i, the sum runs over the 15 reliable bending modes (Mode-4 through Mode-18), and the weights are defined as:

$$w_i = \frac{\min(f_{exp,i}/\Delta f, 100)}{f_{exp,i}^{\alpha}}, \quad \text{normalized so that } \sum w_i = 1 \tag{3.9}$$

Here Δf = 20 Hz is the spectral resolution and α = 0.5 is a frequency-scaling exponent. The weight formula (3.9) reflects two considerations. The factor $f_{exp,i}/\Delta f$ penalizes modes with poor relative frequency resolution: Mode-4 at 1,220 Hz has only 61 resolution cells per frequency, while Mode-18 at 30,320 Hz has 1,516. The factor $1/f^{\alpha}_{exp,i}$ assigns higher weight to lower-frequency modes, where the beam model is most accurate and boundary compliance effects are cleanly separated from higher-order phenomena. With α = 0.5, a mode at 1,220 Hz receives approximately 5 times the weight of a mode at 30,320 Hz.

The theoretical frequencies $f_{theory,i}(L)$ were recomputed at each trial length L by running the full PZT-loaded Timoshenko FEM model (Nel = 320 elements), including PZT mass and stiffness contributions re-evaluated at the

current geometry. This ensures that shear corrections, rotary inertia, and PZT loading are all correctly updated at each candidate length.

The optimization was performed over the range $L \in [0.95L_{nom}, 1.05L_{nom}] = [144.78, 160.02]$ mm. The algorithm converged after 23 function evaluations to $L_{eff} = 152.734$ mm. This represents a +0.334 mm (+0.22%) increase from the nominal length.

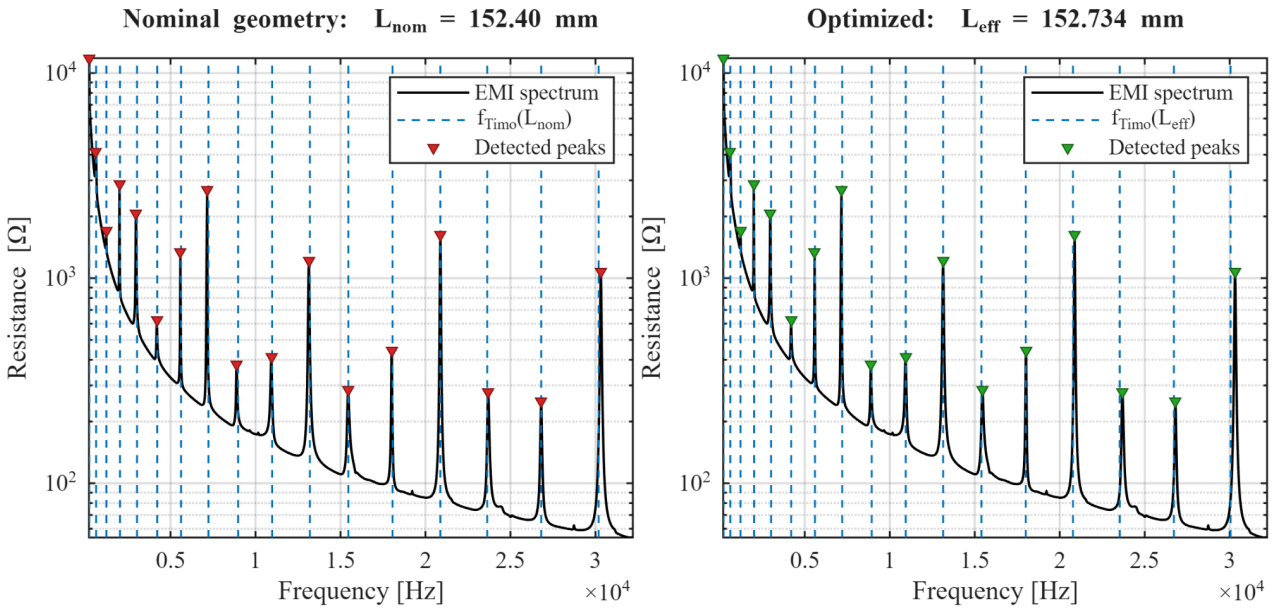

Figure 7. Comparison of experimental EMI resistance spectra (black curve) with theoretical natural frequencies (blue dashed lines). Left: Nominal geometry (L_{nom} = 152.40 mm) showing systematic misalignment where theory overpredicts frequencies. Right: Optimized geometry (L_{eff} = 152.734 mm) showing improved spectral alignment.

A sensitivity study over $\alpha \in [0, 1.5]$ confirms that L_{eff} is stable at ≈ 152.73 mm for $\alpha \leq 0.5$ (spread < 0.004 mm), with the baseline $\alpha = 0.5$ avoiding over-fitting to anomalous low-frequency modes.

The optimization reduced the weighted mean absolute error from 0.80% (Table 1) to 0.553%, representing a 31% improvement. The qualitative improvement in spectral alignment is visualized in Figure 7, where the theoretical predictions (blue dashed lines) shift noticeably closer to the experimental resonance peaks in the right panel. The quantitative mode-by-mode error distribution is shown in Figure 8 (signed errors).

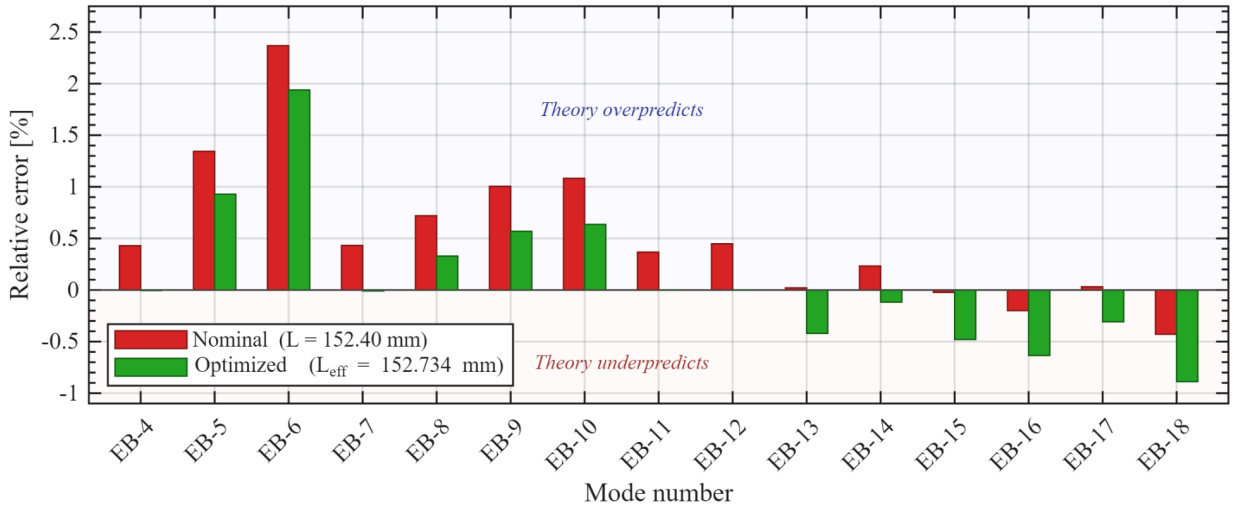

Figure 8. Signed relative error distribution across the identified bending modes for the bolted cantilever beam. The red bars represent the error of the nominal theoretical model L_{nom} = 152.4 mm). The green bars display the residual error following the boundary compliance optimization L_{eff} = 152.734 mm). The effective length extension of ΔL = +0.33 mm collapses the systematic bias and reduces the discrepancies to a lower mean across the measured spectrum.

The improvement is most pronounced in the mid-frequency range, with several modes matched to within 0.01%. The residual errors exhibit a sign reversal - positive at low frequencies (Mode-5: +0.93%, Mode-6: +1.94%) and negative at high frequencies (Mode-18: −0.89%) - reflecting frequency-dependent effects beyond the single-parameter length correction. For reference, a bare-beam optimization (neglecting PZT contributions) yields a weighted error of 0.60%, confirming that including the sensor mass and stiffness improves prediction accuracy.

The positive correction ΔL = +0.33 mm (0.22% of beam length) places the effective fixity point within the clamped region, displaced outward by the rotational compliance of the bolted interface[14]. This magnitude is consistent with boundary compliance values reported for bolted cantilever joints[1,14] and confirms that the fixture provides a well-controlled boundary condition suitable for on-orbit measurements.

3.2. Plate vibration experiments

The cantilever beam study of Section 3.1 was designed as a deliberate one-dimensional simplification of the actual flight article. The sensing element of the MISSE SHM payload is a two-dimensional plate of the same Al6061-T6 aluminum alloy, sharing a characteristic dimension with the beam by design: the plate's active span of 152.4 mm between the bolt rows equals the nominal beam length of 152.4 mm (6.00 inches). This dimensional equivalence allows the boundary compliance correction identified for the beam (ΔL = +0.33 mm), Section 3.1 to serve as a direct quantitative prediction for the plate edge behavior under the same bolted fixation.

The transition from a 1D to a 2D structure introduces modal complexity that cannot be captured by a beam model: coupled bending and torsional modes, two independent boundary directions, and a distributed two-sensor array. To characterize the boundary condition effect on the plate dynamics, two experiments are conducted on the same specimen: a free-suspension baseline and a payload-mounted configuration reproducing the flight boundary conditions. Critically, this is the actual flight article - the plate is characterized on the ground and subsequently integrated into the payload for ISS deployment. All EMI measurements are performed using the Afalina miniaturized electromechanical impedance analyzer, the same instrument that will operate on the International Space Station.

The plate geometry is shown in Figure 9 (a). The specimen outer dimensions are 228.6 mm × 177.7 mm (9.000″ × 6.996″); the active vibrating area between the bolt rows is 203.2 mm × 152.4 mm. The plate thickness is h = 1.016 mm (0.040 inches), identical to the beam specimen. Two APC 850 PWAS transducers (properties as in Section 3.1.1) are bonded to the plate surface in a centro-symmetric arrangement: PWAS-1 is located 50 mm from the top and left edges, and PWAS-2 at the diagonally opposite location, 50 mm from the bottom and right edges. This layout ensures that no plate bending mode is simultaneously nodal at both sensor locations, guaranteeing modal observability across the full measurement range[2].

The payload fixture clamps the plate along all four edges using M3.5×0.6 bolts: 16 bolts along each long edge (203.2 mm span), 12 bolts along each short edge (152.4 mm span), and 4 corner fasteners, for a total of 64 bolted connections. The payload fixture clamps the plate along all four edges using M3.5×0.6 bolts: 16 bolts along each long edge, 12 along each short edge, and 4 corner fasteners, for a total of 60 bolted connections. Four additional unbolted through-holes at the center of each edge serve as cable pass-throughs and are not load-bearing. The fastener type and clamping geometry are identical to those of the beam fixture, enabling direct comparison of boundary compliance between the 1D and 2D configurations.

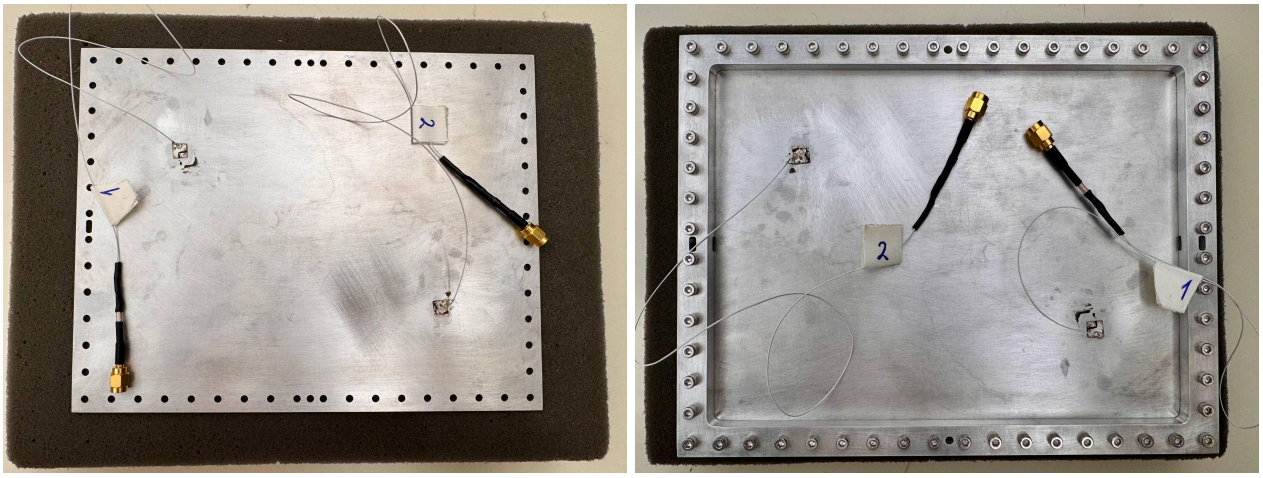

Figure 9. Experimental configurations of the two-dimensional Al6061-T6 flight article sensing plate. **(a)** Free-plate baseline setup, with the specimen resting on a soft foam support to simulate unconstrained boundary conditions. **(b)** Payload-mounted configuration, where the plate is clamped along all four edges by a 64-bolt array (M3.5×0.6) to reproduce the fully clamped (CCCC) flight conditions. The active vibrating area between the bolt rows is 203.2 mm × 152.4 mm. Two APC 850 transducers (PWAS-1 and PWAS-2) are bonded in a centro-symmetric layout to ensure global modal observability.

3.2.1. Theoretical modal analysis

The transverse vibration of a thin, isotropic, homogeneous plate of uniform thickness h is governed by the Kirchhoff–Love equation[13]:

$$D\nabla^4 w + \rho h \frac{\partial^2 w}{\partial t^2} = 0 \tag{3.10}$$

where w(x,y,t) is the transverse displacement, $D = Eh^3/[12(1-\nu^2)]$ is the flexural rigidity, and ∇^4 is the biharmonic operator. Using the material constants of Section 3.1 (E = 68.9 GPa, ρ = 2700 kg/m^3, ν = 0.33, h = 1.016 mm), the flexural rigidity is D = 6.758 N · m.

Kirchhoff analytical baseline. Analytical frequency baselines for both the free (FFFF) and fully clamped (CCCC) configurations are obtained via the Rayleigh–Ritz method, expanding the transverse displacement into products of 1D beam characteristic functions[15]:

$$w(x,y) = \sum_{m=0}^{M} \sum_{n=0}^{N} C_{mn}\, \phi_m\left(\frac{x}{a}\right)\, \psi_n\left(\frac{y}{b}\right) \tag{3.11}$$

where C_{mn} are the amplitude coefficients, and ϕ_m, ψ_n are the appropriate beam eigenfunctions (free–free for FFFF with overall dimensions a = 228.6 mm, b = 177.7 mm; clamped–clamped for CCCC with active dimensions a = 203.2 mm, b = 152.4 mm). For the clamped plate, a single-term Rayleigh-Ritz approximation yields frequency estimates of the form[16]:

$$f_{mn} \approx \frac{1}{2\pi}\sqrt{\frac{D}{\rho h}}\left[\left(\frac{\lambda_m}{a}\right)^2 + \left(\frac{\lambda_n}{b}\right)^2\right] \tag{3.12}$$

where λ_m, λ_n are the eigenvalues of the clamped–clamped beam equation. This expression provides a first-order analytical check against the experimental data.

While these analytical formulations are insightful, the Kirchhoff assumption systematically overpredicts natural frequencies at higher mode numbers (e.g., within the 500–6,000 Hz measurement range). This is due to the neglected transverse shear deformation and rotary inertia - precisely the regime where Timoshenko corrections proved necessary for the beam. Indeed, a preliminary full-matrix Kirchhoff Rayleigh–Ritz computation for the free plate yielded a systematic, frequency-dependent error with a slope of +0.54%/kHz against the experiment, which is characteristic of missing shear physics. Therefore, all quantitative frequency predictions and boundary compliance optimizations are performed using a finite element model incorporating shear deformation.

Mindlin–Reissner finite element model. The plate is modeled using four-node quadrilateral (Q4) shell elements based on Mindlin–Reissner first-order shear deformation theory[13], extending the Timoshenko approach of Section 3.1 to two dimensions. Each node carries three degrees of freedom: transverse displacement w and two independent rotations θx, θy. The element formulation employs selective reduced integration - full 2×2 Gauss quadrature for bending and mass contributions, reduced 1×1 quadrature for transverse shear - to prevent shear locking while maintaining bending accuracy[17]. The shear correction factor is $\kappa = 5/6$. The mesh consists of 80×62=4960 elements (5103 nodes, 15309 DOFs), yielding an element size of 2.86×2.87 mm - providing approximately 9 elements per half-wavelength for the shortest spatial period in the measurement range (mode (9,3) at 4,092 Hz), sufficient for Q4 element convergence.

For the FFFF configuration, no displacement constraints are applied, and the eigenvalue solver returns four rigid-body modes at nominally zero frequency. For the CCCC configuration of Section 3.2.3, all translational and rotational DOFs along the four clamped edges are constrained.

Bolt hole geometry. The plate perimeter contains 64 through-holes (62 circular, Ø3.70 mm; 2 obround, 3.70 × 6.35 mm) at a uniform pitch of 12.70 mm serving as bolt clearance features. These holes constitute local mass and stiffness reductions that are incorporated into the FEM via area-fraction scaling: for each element, a 6×6 sub-sampling grid determines the fractional hole overlap f_{hole}, and both stiffness and mass matrices are scaled by $(1 - f_{hole})$. Of the 4,960 elements, 284 (5.7%) overlap with at least one hole, and the mesh-computed total hole area agrees with the exact geometric value to within 0.5%.

PZT sensor integration. The two PWAS transducers are modeled as distributed mass and stiffness patches following the beam approach of Section 3.1.1, with translational inertia, Steiner-augmented rotary inertia, and bending

stiffness contributions applied to overlapping shell elements. The total PZT mass of 2×0.093 g represents 0.17% of the plate mass (109.6 g), and the affected area (18 elements per sensor) is similarly negligible. As shown in the beam analysis, these PZT contributions have a measurable effect on the 1D structure but become insignificant for the 2D plate.

Mode identification. Each computed eigenvector is identified with a mode pair (m,n) by projecting the transverse displacement field $w(x_i,y_j)$ onto the complete set of free–free beam function products $\phi_p(x/a)\,\phi_q(y/b)$, which form a natural basis for rectangular plate modes[16]. The dominant projection coefficient determines the mode assignment. This approach avoids the circularity of frequency-based matching and remains unambiguous even when modes of different order are closely spaced.

3.2.2. Free plate experiment

The free-plate experiment validates the Mindlin FEM against a configuration with known (unconstrained) boundary conditions, isolating the baseline modeling accuracy from any boundary compliance effects - the same verification strategy applied to the beam in Section 3.1.

Experimental setup. The plate was placed on a soft foam support to approximate mathematically free (FFFF) boundary conditions. Electromechanical impedance spectra were acquired simultaneously from both PWAS transducers using a Keysight E4990A impedance analyzer over the frequency range of 500-6,000 Hz, with a resolution of 3.4375 Hz (1,601 points). The close agreement in resonance peak locations between the two sensors confirms global modal coherence across the plate, while the amplitude differences accurately reflect the nodal line geometry at each specific sensor location.

Mindlin FEM validation. Using the finite element model described in Section 3.2.1 - incorporating the explicit 64-hole geometry and smeared PZT sensor properties, alongside nominal material parameters - the theoretical free-plate frequencies were extracted. The model achieves a highly accurate mean absolute error of 0.585% across 27 confidently identified modes in the 967-4,508 Hz range. However, a slight residual trend remains, which is attributed to the cumulative effect of higher-order dynamic phenomena not fully captured by the first-order shear deformation theory.

Shift function correction. The residual errors exhibit a systematic frequency-dependent slope of +0.54%/kHz, attributable to higher-order shear and thickness effects beyond the first-order Mindlin formulation. An empirical linear correction $\Delta f = 0.01560 \cdot f_{exp} - 28.6$ Hz ($\sigma = 6.04$ Hz), fitted with iterative 2σ outlier rejection, reduces the mean absolute error to 0.265% and collapses the residual slope to a negligible -0.016%/kHz. The corrected theoretical frequencies are overlaid on the experimental spectra in Figure 10, confirming close alignment across the full measurement range.

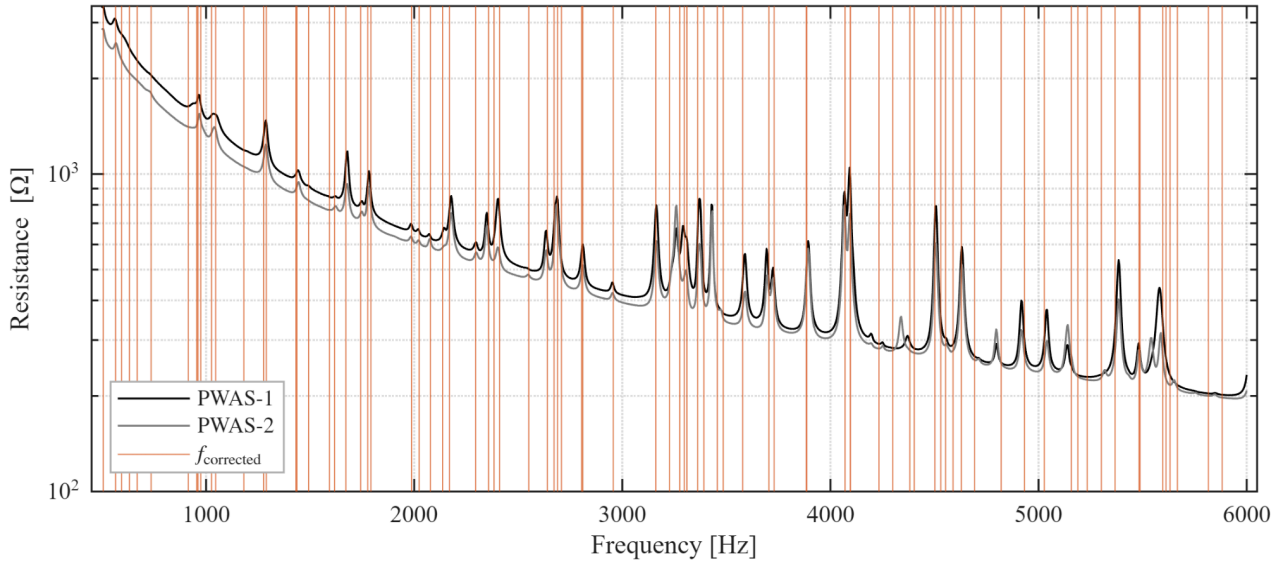

Figure 10. Experimental EMI resistance spectra from PWAS-1 (solid) and PWAS-2 (dashed) under free-plate (FFFF) boundary conditions. Vertical lines indicate the Mindlin FEM predicted natural frequencies after applying the linear shift function, showing exceptional, calibrated alignment with the experimental resonance peaks.

The validated Mindlin FEM and its corresponding shift function thus provide a robust, calibrated theoretical baseline for the clamped boundary analysis in Section 3.2.3, ensuring that the boundary compliance under bolted clamping is quantified against a rigorously verified reference.

3.2.3. Payload-mounted plate experiment and nominal theoretical comparison

In the flight-representative configuration, the plate was installed in the payload fixture and clamped along all four edges with M3.5×0.6 fasteners, reproducing the planned ISS mounting protocol (Figure 9(b)). This boundary condition nominally approximates a fully clamped plate (CCCC), with the 64-bolt perimeter array transmitting bending moments through friction and contact pressure.

EMI spectra were acquired simultaneously from both PWAS transducers using the Keysight E4990A analyzer over the frequency range of 500–6,000 Hz. Figure 11 overlays the resistance spectra from PWAS-1 and PWAS-2. As in the free-plate case (Section 3.2.2), both sensors exhibit consistent modal coherence with complementary amplitude patterns confirming full modal observability.

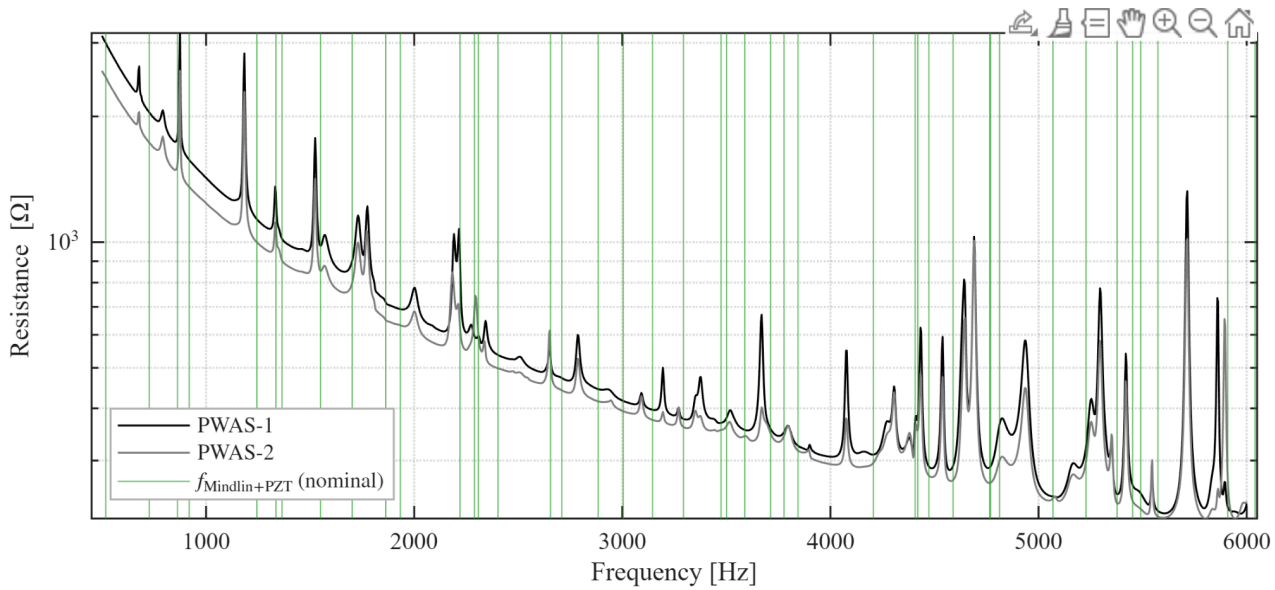

Figure 11: EMI resistance spectra from PWAS-1 (solid) and PWAS-2 (dashed) under payload-mounted (CCCC) boundary conditions. Coincident peak frequencies confirm modal coherence; amplitude differences reflect the nodal line geometry of individual plate modes.

To isolate the physical mechanisms governing the plate's dynamics, the experimental resonance peaks were first compared against nominal theoretical models utilizing the exact active dimensions (a_{nom} = 203.2 mm, b_{nom} = 152.4 mm). Nine dominant bending modes were confidently identified within the 450–2,000 Hz band. The classical Kirchhoff analytical baseline (Eq. 3.12) systematically overpredicted the frequencies with a severe mean absolute error of 17.38%. Transitioning to the nominal Mindlin+PZT finite element model reduced this mean absolute error dramatically to 5.90%, mathematically isolating and confirming the necessity of including transverse shear deformation for thin plates in the high-frequency SHM regime.

However, the nominal Mindlin FEM still exhibited a consistent positive frequency shift across all modes (e.g., the fundamental (2,1) mode: 518.0 Hz predicted vs. 480.1 Hz measured). Since shear deformation and PZT effects are already captured in the model, this residual 5.90% overprediction is attributed to the boundary compliance of the bolted frame — the same mechanism identified for the beam in Section 3.1.3.

3.2.4. Optimization of effective plate dimensions

To quantify the compliance of the bolted fixture, the effective-length approach of Section 3.1 is extended to two parameters: the effective active dimensions a_{eff} and b_{eff}. The weighted cost function is defined as:

$$J(a_{\text{eff}}, b_{\text{eff}}) = \sum_{m,n} w_{mn} \left[\frac{f_{\text{FEM},mn}(a_{\text{eff}}, b_{\text{eff}}) - f_{\text{exp},mn}}{f_{\text{exp},mn}} \right]^2 \tag{3.13}$$

where theoretical frequencies $f_{FEM,mn}(a_{eff}, b_{eff})$ are recomputed at each trial geometry by executing the full PWAS-loaded Mindlin FEM. The optimization yielded effective dimensions of a_{eff} = 209.47 mm and b_{eff} = 156.37 mm. This corresponds to an effective span increase of Δa = +6.27 mm (+3.09%) and Δb = +3.97 mm (+2.61%). By adopting these effective dimensions, the theoretical model was brought into good agreement with the experimental specimen, driving the mean absolute error down from 5.90% to just 2.38%.

Unlike the wideband beam optimization (where a frequency-scaling exponent α = 0.5 was necessary to mitigate higher-order shear uncertainties at frequencies up to 30 kHz), the targeted bending modes for the CCCC plate fall within a much narrower and lower frequency band (450–2,000 Hz). In this regime, shear deformation uncertainties are minimal. Consequently, the weights w_{mn} were assigned based purely on relative spectral resolution (α = 0), defined as $w_{mn} \propto f_{exp,mn} / \Delta f$. This approach naturally prioritizes modes with higher frequency resolution density, ensuring the boundary compliance optimization is driven by the most sharply defined experimental peaks.

Physically, these corrections quantify the boundary penetration depth: the dynamic bending modes penetrate approximately 2.0 to 3.1 mm per side into the 12.7 mm clamped margins beneath the bolted frame before encountering an effective fixed boundary. This finite compliance at nominally clamped edges is consistent with the rotational boundary correction described by Hu and Adams[18], who showed that elastic deformation within clamped supports produces frequency shifts comparable to or greater than shear deformation effects. Initially, based on identical fastener types and applied torques, the 2D dimensional compliance was hypothesized to match the 1D beam result ($\Delta L/L_{nom} \approx$ 0.22%). However, the optimized 2D compliance (~3%) is an order of magnitude larger. This deviation reflects a fundamental difference in boundary mechanics: the aggregate compliance of a 60-bolt perimeter array, governed by discrete contact zones and inter-bolt frame flexibility, differs substantially from the continuous clamping provided by a single monolithic block. The overlaid optimized theoretical frequencies show strong agreement with the experimental resistance peaks across the high-density modal spectrum, confirming the physical validity of the effective-dimension approach (Figure 12).

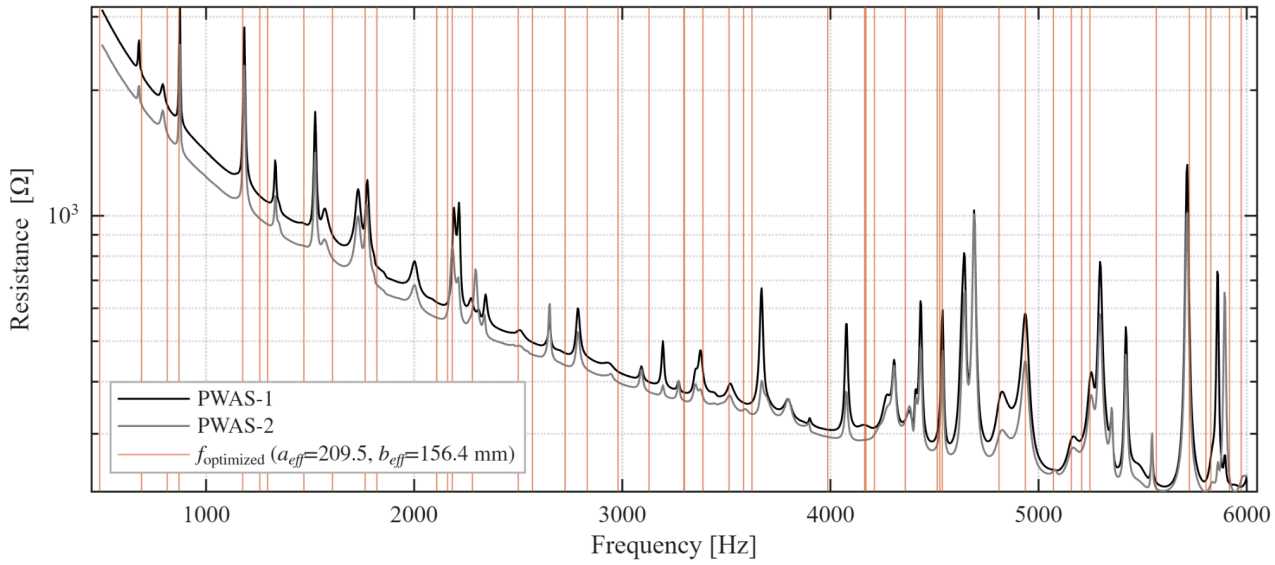

Figure 12. Experimental EMI resistance spectra from PWAS-1 (solid) and PWAS-2 (dashed) for the payload-mounted plate, overlaid with the natural frequencies predicted by the boundary-optimized Mindlin finite element model (vertical lines). By scaling the effective active dimensions to a_{eff} = 209.47 mm and b_{eff} = 156.37 mm, the theoretical model successfully captures the compliance of the 60-bolt perimeter array, resulting in a highly accurate modal alignment (2.38% mean error) across the targeted high-frequency band.

3.2.5. Afalina impedance analyzer verification

The theoretical model developed in Sections 3.2.1–3.2.4 was validated using laboratory-grade Keysight E4990A measurements to ensure the highest possible frequency resolution and measurement fidelity. However, the in-orbit EMI data will be acquired by the Afalina miniaturized impedance analyzer (Section 2.3.1). To confirm that the Afalina instrument provides spectra consistent with the calibrated theoretical baseline, a verification measurement was performed on the payload-mounted (CCCC) plate using the Afalina analyzer over the same frequency range of 500–6,000 Hz with identical frequency resolution ($\Delta f = 3.4375$ Hz).

While the absolute impedance magnitudes differ between the miniaturized Afalina analyzer and the laboratory-grade Keysight E4990A due to differing excitation power levels and hardware architectures, this discrepancy is strictly a cross-instrument scaling artifact. For the duration of the orbital mission, all diagnostic spectra will be consistently acquired by the Afalina hardware. Within this self-referential operational framework, the Afalina analyzer is fully capable of accurately tracking relative shifts in both resonance frequencies and impedance amplitudes induced by structural degradation. The critical verification metric is therefore the alignment of the resonant peak frequencies between the two instruments.

The raw Afalina spectra exhibit visible ADC quantization noise, particularly at low frequencies where the structural impedance is dominated by the capacitive baseline and the signal-to-noise ratio is reduced. To suppress these digitization artifacts without distorting the modal content, a 5-point moving average was applied to the Afalina trace, corresponding to a smoothing window of approximately 17 Hz which is well below the typical resonance peak width in this frequency range.

To quantify this alignment, 28 resonance peaks were independently identified in the Keysight and Afalina spectra across the 500–6,000 Hz range and matched pair-wise. Figure 13 overlays the normalized resistance spectra from both instruments for PWAS-1 (each normalized to its own maximum), confirming visual correspondence of all major resonance features. The cross-instrument frequency discrepancy statistics: the mean absolute deviation is 9.1 Hz (0.44%), the median absolute deviation is 6.9 Hz (approximately two frequency resolution steps), and 71% of the

matched peaks fall within ±3 resolution steps (±10.3 Hz). Above 3,000 Hz, the agreement tightens further, with 17 of 18 peaks differing by less than 0.42%. Two low-frequency peaks near 792 Hz and 1,184 Hz exhibit deviations exceeding 2%, likely attributable to the lower signal-to-noise ratio of the miniaturized hardware at frequencies where the structural impedance is dominated by the capacitive baseline. Excluding these two outliers, the remaining 26 peaks yield a mean frequency discrepancy of 0.30%.

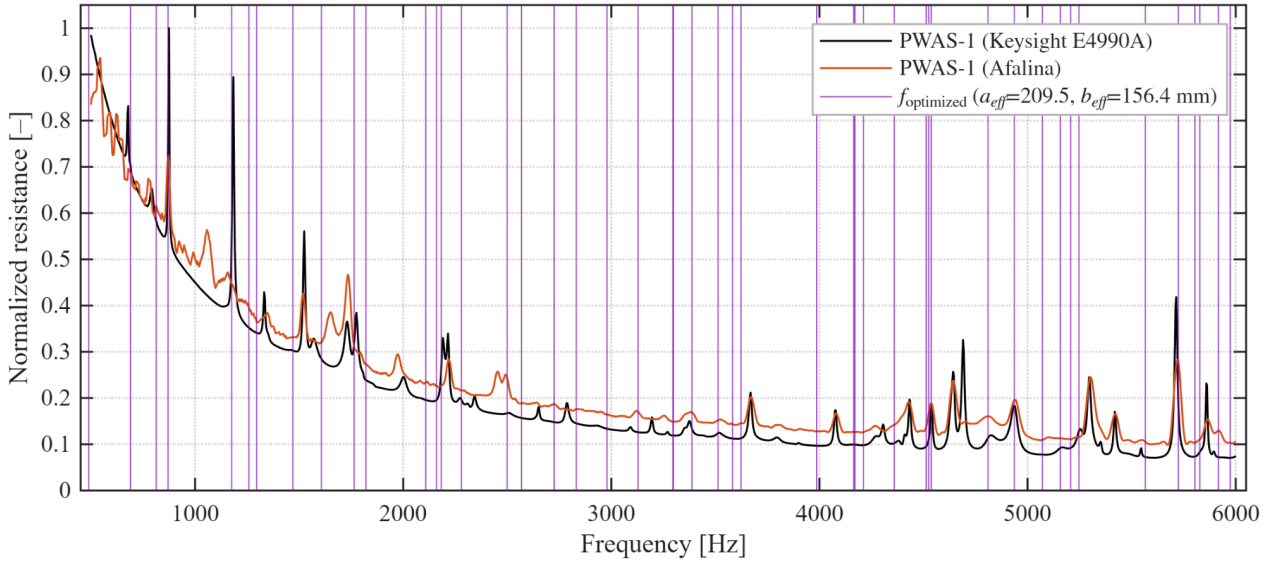

Figure 13. Normalized resistance spectra from PWAS-1 acquired by the Keysight E4990A (black) and Afalina miniaturized analyzer (orange), overlaid with the boundary-optimized Mindlin FEM predictions (a_{eff} = 209.47 mm, b_{eff} = 156.37 mm, purple). Each spectrum is normalized to its maximum value; a 5-point moving average (~17 Hz window) is applied to the Afalina trace to suppress ADC quantization noise. The alignment of resonance peaks across the full frequency range confirms modal coherence between the two instruments.

This sub-percent cross-instrument agreement establishes that the ground-based theoretical baseline developed from Keysight measurements can be directly compared against in-orbit Afalina data without introducing systematic frequency bias. The Afalina spectra thus serve as the validated operational pre-flight reference against which all orbital EMI measurements will be evaluated.

4. GUIDED WAVE EXPERIMENT

Structural health monitoring (SHM) via guided wave propagation has seen widespread adoption in aerospace applications due to its sensitivity to small-scale damage and ability to interrogate large structural areas from a limited number of sensor nodes [23]. This work employs mechanical Lamb waves to characterize an aluminum plate substrate and detect damage through analysis of acoustic response spectra.

A data-driven modeling framework was selected over physics-informed or direct analytical Lamb wave models for several reasons pertinent to this experimental configuration. Aerospace structures are typically complex geometries with boundary conditions that make direct Lamb wave modeling difficult and computationally complex [16]. In the experimental payload, reflections from plate edges introduce significant reverberation and coherent noise in the active response signals, making analytical inversion unreliable. Data-driven methods naturally accommodate this complexity and integrate well with machine learning inference pipelines [17], enabling computationally efficient damage classification.

4.1. Guided wave theory

A Lamb wave is an elastic guided wave that propagates within a thin plate whose thickness is on the order of the acoustic wavelength. Lamb waves manifest in two fundamental mode families: symmetric (S) modes, in which particle motion is symmetric about the plate midplane, and anti-symmetric (A) modes, in which particle motion is antisymmetric. Each mode family disperses at a frequency- and thickness-dependent group velocity, which can be represented graphically as a dispersion curve relating group velocity to the frequency-thickness product.

For the purposes of this investigation, analysis was restricted to the initial symmetric (S0) and anti-symmetric (A0) modes. These modes are the first to arrive at a receiver node following actuation, exhibit the greatest resistance to dispersion and reverberation noise, and are the most thoroughly characterized in the literature [19]. Limiting extraction to S0 and A0 also reduces computational overhead, an important consideration for the onboard embedded processing architecture.

The symmetric Lamb wave is characterized by same-direction mechanical waveforms on both edges of an infinite plate, creating an extensional wave motion. The anti-symmetric waveform in an infinite plate exists as a flexural motion, with both edges oscillating in opposite directions, as illustrated in Figure 14.

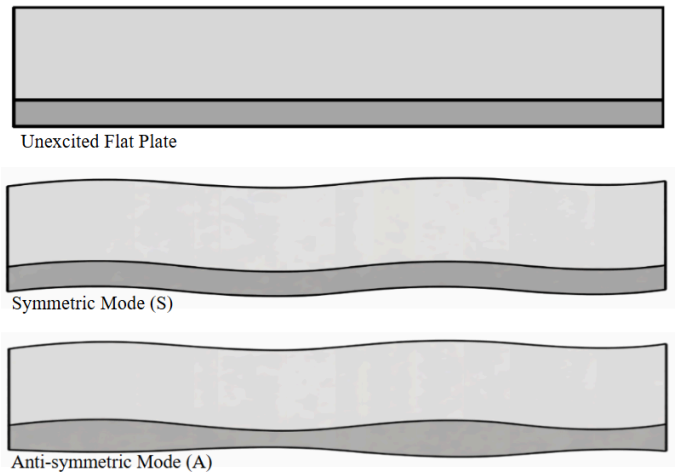

Figure 14. Flat plate visual comparison between symmetric (S) and anti-symmetric (A) wave modes. When a flat thin plate is mechanically excited, two Rayleigh wave shapes appear. The S mode is characterized by extensional motion, while the A mode is represented by flexural motion.

For analytical structural health monitoring, it is useful to analyze typical Lamb wave velocities through a thin plate. Theoretical Lamb wave phase velocities in an isotropic plate can be derived from the Lamé elastic constants as follows:

$$\mu = \frac{E}{2(1+\nu)} \tag{4.1}$$

$$\lambda = \frac{E\nu}{(1-2\nu)(1+\nu)} \tag{4.2}$$

Here, λ and μ are the first and second Lamé parameters. These are defined by isotropic material properties, where E is the elastic modulus of a solid, and ν is the Poisson's ratio of a material. These properties are well defined for most experimental substrates, and well studied for aluminum 6061-T6. These parameters can then be used to identify the longitudinal and transverse Lamb bulk wave speeds in a material:

$$c_t^2 = \frac{\mu}{\rho} \tag{4.3}$$

$$c_l^2 = \frac{(\lambda + 2\mu)}{\rho} \tag{4.4}$$

In these equations, cl and ct are the longitudinal and transverse wave speeds, respectively, and ϱ is defined as the density of the substrate material. These bulk wave speeds serve as inputs to the Rayleigh-Lamb dispersion relations, from which theoretical group velocity curves can be computed for comparison and calibration with experimental measurements.

$$c_{group} = \frac{c_p}{1 - (f/c_p)\delta c_p/\delta f} \tag{4.5}$$

Here, group velocity is calculated as a partial differential equation dependent on the parameters of phase velocity (cp) and frequency (f). The group velocity can then be calculated using numerical methods, but for the purpose of this paper, previous characterization of thin aluminum 6061-T6 plates was used as a baseline for the Lamb wave group velocity curves [18]

These equations can calculate hypothetical Lamb wave speed in bulk materials, and are often used as an analytical model to identify deformities of an isotropic material through deviation from expected wave speeds. This can be done by placing two piezoelectric wafers at a known distance apart. One wafer can excite a guided wave into the plate, and the other wafer will act as a receiver node. The time elapsed between the initial excitation and the reading from the receiver node can be used to calculate the wave speed [20].

4.2. Methodology

Guided wave interrogation was performed by placing two piezoelectric wafer active sensors (PWAS) at a known separation on the aluminum plate. A Ritec RAM-5000 high-voltage pulser delivered a controlled burst excitation to the actuator PWAS across a range of interrogation frequencies. The resulting wave packet was recorded at the receiver PWAS, yielding time-domain acoustic spectra from which wave group velocities could be extracted.

Signal processing followed a data-driven approach. A Hilbert transform was applied to each raw waveform to obtain the analytic envelope, isolating the Gaussian amplitude peaks associated with individual wave mode arrivals. Representative time-domain waveforms are shown in Figure 15: at 250 kHz (Figure 15(a)), the ML-based algorithm cleanly identifies S0 and A0 arrivals in the Hilbert envelope, while at 850 kHz (Figure 15(b)), later-arriving modes overlap due to boundary reflections, illustrating the increased complexity at higher interrogation frequencies.

$$\mathrm{H}(u)(t) = \frac{1}{\pi}\ \mathrm{p.v.} \int_{-\infty}^{+\infty} \frac{u(\tau)}{t - \tau}\,\mathrm{d}\tau \tag{4.6}$$

The Hilbert transform (Eq. 4.6) was computed numerically using the MATLAB Signal Processing Toolbox.

4.3. Results and comparison to guided wave theory

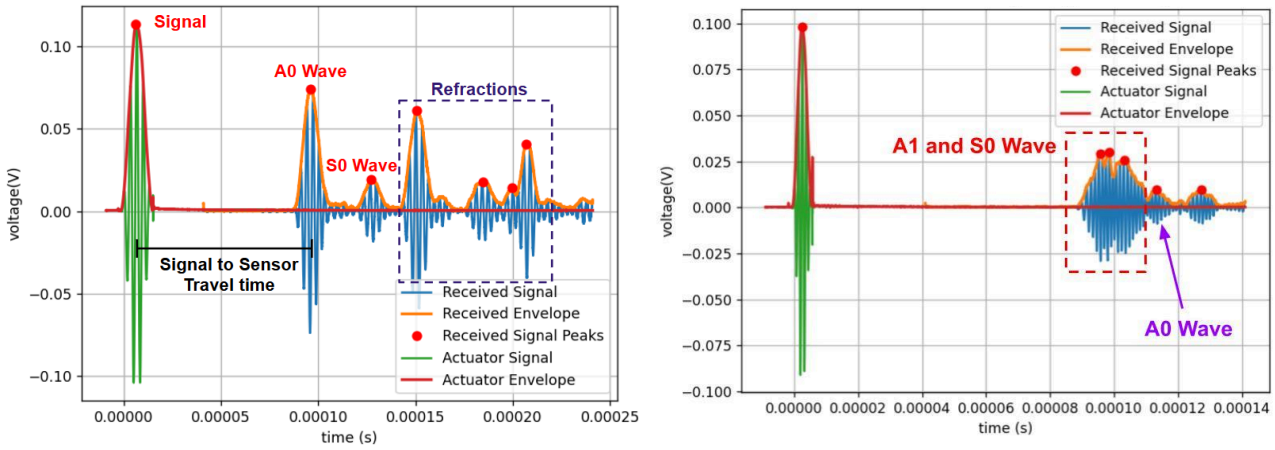

Figure 15. (a) 250 kHz Interrogation. The ML-based signal processing algorithm detected peaks in the Hilbert envelope to find node-to-node guided wave travel time. Data for later-arriving wave modes can be cluttered, as refractions with plate boundaries occur before A_1 or S_1 modes **(b)** 850 kHz Interrogation. At higher frequencies, it can be more difficult to pick out cluttered waveforms as the A_1 wave arrives before the A_0 wave.

The resulting dispersion data were compared against theoretical curves computed for a 1 mm-thick Aluminum 6061 plate, as shown in Figure 16. Good agreement was observed at higher frequency-thickness products, validating the sensor baseline and the signal processing pipeline. Deviations at lower frequencies are attributed to the finite plate dimensions of the experimental specimen, which violate the infinite-plate assumption underlying the Rayleigh-Lamb equations.

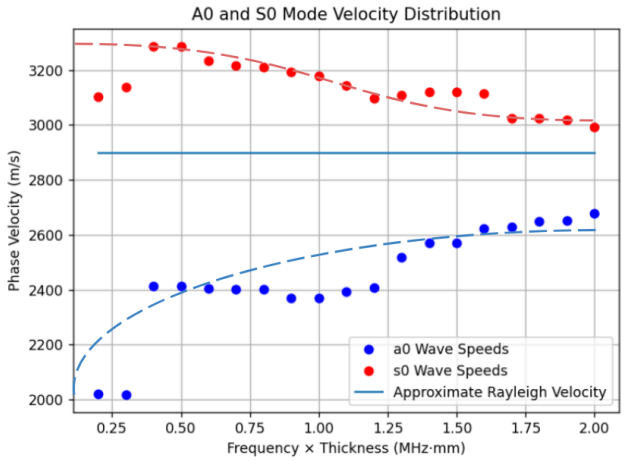

Figure 16. Comparison between theoretical Rayleigh-Lamb approximation for phase velocity, plotted against experimentally derived values. Experimental values were calculated using signal speed between PWAS nodes. The Rayleigh-Lamb approximations generally overpredict wave speeds at low frequencies between 0 and 150 kHz through a 1-mm plate as compared to experimental values.

At higher interrogation frequencies, the A1 wave mode is present in thin aluminum plates, with a group velocity exceeding that of the A0 mode, as visible in the 850 kHz waveform of Figure 15(b). This introduces an additional arrival that precedes the A0 mode at the receiver. To account for this, the modal assignment was updated above the A1 cutoff frequency: the first-arriving packet was classified as A1, the second as S0, and the third as A0. This adjustment was incorporated into the machine learning peak identification algorithm. At around 2 MHz·mm, above the A1 cutoff

frequency, the algorithm was updated based on the theoretical group velocity dispersion curves, assigning the first-arriving packet to A1.

In order to enable accurate readings from each PWAS sensor, the impedance characteristics of each PWAS node were measured. This will allow accurate baseline readings to adjust data from each node during experimentation. Prior to integration, each PWAS node was characterized using a Keysight E4990A impedance analyzer to determine its natural resonance frequency and confirm electromechanical performance.

Impedance measurements were acquired across three frequency bands: 7–10 MHz, 250–400 kHz, and 350–800 kHz. Total impedance magnitude and phase angle were computed from the measured real (R) and reactive (X) components:

$$|Z| = \sqrt{R^2 + X^2} \tag{4.7}$$

$$\phi = arctan\left(\frac{X}{R}\right) \tag{4.8}$$

Both phase and impedance magnitude were calculated for each PWAS node on the aluminum plate. This was accomplished using point-wise operations on input real and imaginary impedance data from the Keysight E4990A.

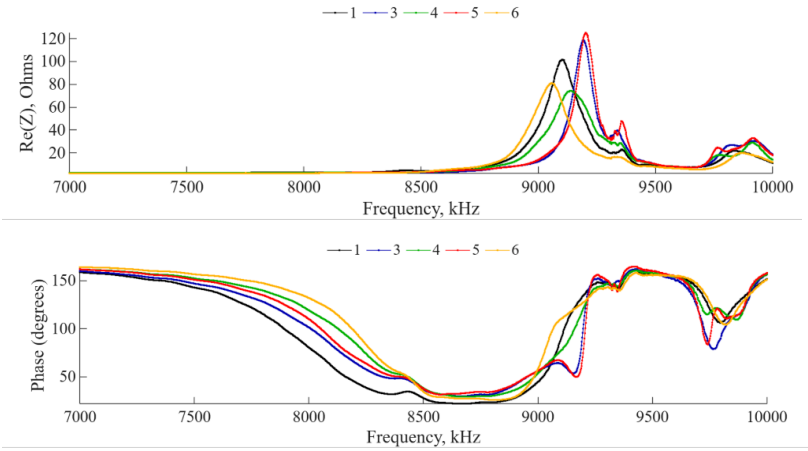

Figure 17. Impedance and phase readings across the 7-10MHz frequency band. Each PZT wafer showed a natural frequency between the 9.0 and 9.3 MHz range, which was verified through phase readings across the same frequency band.

The five PWAS nodes exhibited a mean resonance frequency of 9.085 MHz with a standard deviation of 53 kHz, consistent with manufacturer specifications. The observed spread is expected given the small sample size and is within acceptable bounds for calibrated guided wave excitation. Sensor 2 is not included in the diagrams, as sensor 2 was used as the external PZT sensor after characterization. Readings across the 250 to 850 kHz frequency range showed a similar characteristic distribution as those presented in Figure 17.

During the six-month orbital mission, guided wave interrogation will be performed once per week using the Metis Design MD7 microcontroller, which manages PWAS actuation and data acquisition autonomously. A total of 24 guided wave data sets will be collected across the mission duration, sampling a range of orbital thermal environments as the payload traverses different regions of the Earth's orbit. Because the dielectric and mechanical properties of PZT transducers are temperature-dependent, data collected at varying ambient temperatures will provide an opportunity to

study thermally induced variation in wave speed and sensor response, which are important considerations for developing in-situ baseline correction algorithms for space-based SHM systems.

5. PAYLOAD VALIDATION AND CONCLUSION

5.1. Conclusion

This paper presented the design, theoretical modeling, and on-Earth characterization of a PWAS-based structural health monitoring payload to be deployed to the International Space Station via the MISSE platform. Two SHM methods—electromechanical impedance (EMI) and guided wave propagation—have been implemented on Al6061-T6 aluminum plate substrates to represent aerospace structural panels, and thorough pre-flight characterization of actual flight hardware has been completed.

A hierarchical modeling strategy was developed to characterize the bolted boundary conditions of the experimental EMI aluminum plate. Beginning with a one-dimensional cantilever beam sharing the same fastener type, edge geometry, and material as the payload plate, a PZT-equipped Timoshenko finite element model predicted 15 bending modes over the range of 1,220 to 30,320 Hz with a mean absolute error of 0.80% at nominal dimensions. Single-parameter effective length optimization reduced this error to 0.553%, identifying an effective fixity offset of $\Delta L = +0.33$ mm (+0.22%) that quantifies the rotational compliance of the bolted joint. This verified that the fixture provides a reproducible boundary condition and established a 1D baseline compliance metric.

This one-dimensional analysis was subsequently extended to the two-dimensional payload plate using a Mindlin–Reissner finite element model incorporating exact bolt-hole geometry and smeared PZT sensor properties. Validated against a free-plate experiment, the model achieved a mean absolute error of 0.265% across 27 modes after applying a linear shift-function correction. For the payload-mounted (CCCC) configuration, the nominal Mindlin FEM systematically overpredicted the experimental frequencies, yielding a 5.90% mean error. A two-parameter effective dimension optimization successfully compensated for this discrepancy, minimizing the error to 2.38% by identifying effective span increases of $\Delta a = +6.27$ mm (+3.09%) and $\Delta b = +3.97$ mm (+2.61%). Crucially, this optimization revealed that the dynamic boundary compliance of the 64-bolt 2D perimeter array (~3%) is an order of magnitude larger than that of the 1D monolithic clamp (~0.22%), demonstrating that complex multi-bolted joint mechanics cannot be purely extrapolated from simplified 1D tests. This cross-validated, physically grounded model now serves as the highly accurate baseline for in-orbit EMI data interpretation.

Verification measurements with the flight Afalina impedance analyzer confirmed that the miniaturized instrument reproduces the modal content of the Keysight-calibrated baseline: across 28 matched resonance peaks spanning 500–6,000 Hz, the mean cross-instrument frequency discrepancy was 0.44%, improving to 0.30% when two low-frequency peaks affected by reduced signal-to-noise ratio were excluded. This sub-percent agreement establishes a continuous measurement chain from the laboratory reference through the in-orbit data acquisition hardware without systematic frequency bias.

A data-driven guided wave characterization framework was developed and validated on the flight plate prior to integration. Experimental group velocity dispersion curves showed good agreement with theoretical Rayleigh-Lamb predictions for a 1 mm Al6061-T6 plate at higher frequency-thickness products. Experimental low-frequency deviations are attributable to the finite plate geometry, though the Rayleigh-Lamb predictions overestimate experimentally obtained values. Pre-flight PWAS characterization confirmed a mean resonance frequency of 9.085 ± 0.053 MHz across the five-sensor array, consistent with manufacturer specifications and suitable for calibrated broadband excitation. These experiments provide baseline characterization of the PZT wafers for pre-flight control data.

Together, the EMI and guided wave ground characterization results establish a detailed pre-flight baseline against which in-orbit measurements will be compared. The payload will collect 24 guided wave data sets and periodic EMI spectra over its six-month mission, sampling a range of orbital thermal environments from −65°C to +125°C. By tracking changes of resonant frequencies, modal shifts, and wave group velocities relative to the ground baseline, the experiment will provide the first in-situ characterization of PZT transducer performance and guided wave propagation

behavior in the LEO environment. These results are expected to inform the development of thermally compensated SHM algorithms and in-orbit sensor degradation models for future space vehicle SHM systems.

[1] Ibrahim, R. A. and Pettit, C. L., “Uncertainties and dynamic problems of bolted joints and other fasteners,” J. Sound Vib. **279**(3–5), 857–936 (2005).

[2] Giurgiutiu, V., [Structural Health Monitoring with Piezoelectric Wafer Active Sensors, 2nd edition], Academic Press (2014).

[3] Park, G., Sohn, H., Farrar, C. R. and Inman, D. J., “Overview of Piezoelectric Impedance-Based Health Monitoring and Path Forward,” Shock Vib. Dig. **35**(6), 451–463 (2003).

[4] Hunter, D. C., “Adaptation of electro-mechanical impedance structural health monitoring for use in spacecraft,” Master’s thesis (2018).

[5] Analog Devices., “AD5940/AD5941 Datasheet,” <https://www.analog.com/media/en/technical-documentation/datasheets/AD5940-5941.pdf> (10 February 2026).

[6] ASM international, ed., [ASM handbook: nonferrous alloys and special-purpose materials, 10th ed], ASM international, Materials park (Ohio) (1990).

[7] APC International., “Physical and Piezoelectric Properties of APC Materials,” APC Int. Ltd Mackeyville PA, March 2026, <https://www.americanpiezo.com/apc-materials/physical-piezoelectric-properties/>.

[8] Rao, S. S., [Vibration of Continuous Systems, 1st ed.], Wiley (2006).

[9] Blevins, R. D., [Formulas for Natural Frequency and Mode Shape], Van Nostrand Reinhold, New York (1979).

[10] Timoshenko, S. P., “On the correction for shear of the differential equation for transverse vibrations of prismatic bars,” Philos. Mag. **41**(245), 744–746 (1921).

[11] Huang, T. C., “The Effect of Rotatory Inertia and of Shear Deformation on the Frequency and Normal Mode Equations of Uniform Beams With Simple End Conditions,” J. Appl. Mech. **28**(4), 579–584 (1961).

[12] Cowper, G. R., “The Shear Coefficient in Timoshenko’s Beam Theory,” J. Appl. Mech. **33**(2), 335–340 (1966).

[13] Logan, D. L., [A first course in the finite element method, Sixth edition, SI], Cengage learning, Boston (2017).

[14] Ahmadian, H. and Jalali, H., “Identification of bolted lap joints parameters in assembled structures,” Mech. Syst. Signal Process. **21**(2), 1041–1050 (2007).

[15] Leissa, A. W., [Vibration of Plates], Scientific and Technical Information Division, National Aeronautics and Space Administration, Washington, D.C. (1969).

[16] Warburton, G. B., “The Vibration of Rectangular Plates,” Proc. Inst. Mech. Eng. **168**(1), 371–384 (1954).

[17] Hughes, T. J. R., Cohen, M. and Haroun, M., “Reduced and selective integration techniques in the finite element analysis of plates,” Nucl. Eng. Des. **46**(1), 203–222 (1978).

[18] Hu, D. and Adams, G. G., “A boundary condition correction for the clamped constraint of elastic plate/beam theory,” Int. J. Solids Struct. **124**, 229–234 (2017).

[16] da Silva, S., L. G. G. Villani, M. R´ebillat, and N. Mechbal. 2021. “Gaussian Process NARX Model for Damage Detection in Composite Aircraft Structures,” Journal of Nondestructive Evaluation, Diagnostics and Prognostics of Engineering Systems, 5(1), ISSN 2572-3901, 011007

[17]Zhang, Z., H. Pan, X. Wang, and Z. Lin. 2020. “Machine learning-enriched lamb wave approaches for automated damage detection,” Sensors, 20(6):1790.

[18] Rose, J. L. (2014). *Ultrasonic guided waves in solid media*. Cambridge University Press. https://doi.org/10.1017/CBO9781107273610

[19]Sun, X., Ding, X., Li, F., Zhou, S., Liu, Y., Hu, N., Su, Z., Zhao, Y., Zhang, J., & Deng, M. (2018). *Interaction of Lamb wave modes with weak material nonlinearity: Generation of symmetric zero-frequency mode*. *Sensors*, *18*(8), 2451

[20]Kessler, S. S., & Spearing, S. M. (2002). *In-situ sensor-based damage detection of composite materials for structural health monitoring* (AIAA Paper No. 2002-1545). American Institute of Aeronautics and Astronautics. https://doi.org/10.2514/6.2002-1545

[21]Kang, S.-Y., Jo, M.-S., Choi, J.-Y., & Yang, S. S. (2025). *Cost Effectiveness of Reusable Launch Vehicles Depending on the Payload Capacity*. Aerospace, **12**(5), 364. https://doi.org/10.3390/aerospace12050364

[22]C.S. Wang, F.-K. Chang, (2000) *Diagnosis of impact damage in composite structures with built-in piezoelectrics network*, Proceedings of SPIE Smart Structures and Materials: Smart Electronics and MEMS 3990, Newport Beach, USA

[23]Ajay Raghavan and Carlos E. S. Cesnik (2007) *Review of Guided-wave Structural Health Monitoring*. The Shock and Vibration Digest; 39; 91 DOI: 10.1177/0583102406075428